SAND2017-11361C

Interface Reduction on Hurty/Craig-Bampton Substructures with Frictionless Contact

Patrick J. Hughes[1], Wesley Scott[2], Wensi Wu[3], Robert J. Kuether[4], Matthew S. Allen[2], Paolo Tiso[5]

[1]Department of Structural Engineering, University of California - San Diego, La Jolla, California 92093, USA
[2]Department of Engineering Physics, University of Wisconsin - Madison, Madison, Wisconsin 53706, USA
[3]School of Civil and Environmental Engineering, Cornell University, Ithaca, New York 14850, USA
[4]Sandia National Laboratories, Albuquerque, New Mexico 87185, USA
[5]Institute for Mechanical Systems, ETH Zurich, 8092 Zurich, Switzerland

---

Abstract

Contact in structures with mechanical interfaces has the ability to significantly influence the system dynamics, such that the energy dissipation and resonant frequencies vary as a function of the response amplitude. Finite element analysis is commonly used to study the physics of such problems, particularly when examining the local behavior at the interfaces. These high fidelity, nonlinear models are computationally expensive to run with time-stepping solvers due to their large mesh densities at the interface and because of the high expense required to update the tangent operators. Hurty/Craig-Bampton substructuring and interface reduction techniques are commonly utilized to reduce computation time for jointed structures. In the past, these methods have only been applied to substructures rigidly attached to one another, resulting in a linear model. The present work explores the performance of a particular interface reduction technique (system-level characteristic constraint modes) on a nonlinear model with node-to-node contact for a benchmark structure consisting of two c-shape beams bolted together at each end.

Keywords: Component Mode Synthesis, Substructuring, Hurty/Craig-Bampton Method, Interface Reduction, Mechanical Joints, Contact

---

1. Introduction

Contact in structures with mechanical interfaces can have a significant influence on the dynamic response to time varying loads. The magnitude of clamping forces near the contact due to bolt preloads influences the overall stiffness in the system, while frictional effects in joints typically contribute to the overall structural damping [1]. A common approach in interface modeling is to approximate contact areas with linear springs and dashpots, or with nonlinear

elements such as Jenkins elements [2] or Iwan elements [3]. These approaches are capable of simplifying the interface model at the expense of losing local kinematics and stresses at these locations. When higher interface fidelity is desired, the interfaces must be modeled in full detail with a fine mesh resolution to adequately resolve nonlinear contact and friction effects. Sophisticated models of this type are computationally expensive to run with transient solvers, due to the high number of degrees-of-freedom (DOF) required to accurately capture the local contact forces at the interface. Furthermore, the contact state can change in time, requiring continuous updating of internal force vectors and Jacobian operators within implicit integration schemes. This work seeks to address this issue by exploring model order reduction techniques to speed up transient simulations for structures with nonlinear contact. The current study focuses on the frictionless case such that there are no tangential loads due to friction.

Component mode synthesis (CMS) methods in structural dynamics are used to reduce the linear portion of a model, while preserving the physical DOF at interfaces containing nonlinear elements [4,5]. One commonly used approach is the Hurty/Craig-Bampton (HCB) method, which was originally proposed by Hurty [6], and later simplified by Craig and Bampton [7]. The HCB method represents each subcomponent by a truncated set of dynamic fixed-interface modes, augmented with a static constraint mode for every physical interface DOF. For finite element models with a fine interfacial mesh, the number of constraint modes needed for the HCB method becomes excessively high and prohibits the effectiveness for applications involving contact. Furthermore, the critical time step for HCB models with explicit time solvers is dictated by the static constraint modes, which are localized in shape and therefore associated with high frequencies. As such, model reduction does little if anything to improve this [4].

The objective of this research is to further decrease the HCB model order by performing a secondary reduction on the interface DOF using a set of mode shapes describing the interface kinematics. Some of the authors have recently reviewed interface reduction methods for HCB models in [8], but these techniques were only applied to linear substructures with rigid compatibility enforced (i.e. linear assembly models). The review paper reveals that the system-level characteristic constraint mode method originally developed by Craig and Chang [9], and later elaborated by Castanier et al. [10] is most accurate for rigidly connected boundary DOF. This modal basis is slightly modified in this work to preserve some of the physical boundary DOF in the subspace. A few other works have explored interface reduction techniques on contacting interfaces. Becker and Gaul [5] applied component mode synthesis to structure with bolted joints, but the number and type of interface modes needed to resolve the local and global response remains an open research question.

In this research, the HCB method with a modified version of system-level interface reduction [9,10] is used to model a system consisting of two C-shape beams bolted together at each end (see Figure 1 in Section 3.1). Interface contact is considered frictionless here, modeled using node-to-node penalty springs [11] in the normal direction only. This work examines the necessary interface basis vectors to resolve the nonlinear kinematics at the frictionless contacting surfaces. Furthermore, this research examines the effect of interface reduction on transient solution accuracy and simulation time, relative to the full-interface HCB model.

2. Theory

2.1. Nonlinear Hurty/Craig-Bampton Method

Modern finite element models tend to have extremely fine meshes, with potentially hundreds of thousands of elements and millions of DOF. In models with substructures connected to one another via contacting boundary conditions, the interface DOF may control the dynamic response of the system, while the numerous interior (non-interface) DOF provide unnecessary model redundancy. As such, the interior DOF can be reduced through CMS methods, which approximate the substructure interior with a relatively small set of mode shapes, while leaving the interface DOF unchanged. One such method is the Hurty/Craig-Bampton technique, summarized below for the case when substructures are connected through nonlinear contact elements.

Consider an arbitrary substructure in an assembly with nonlinear elements at the interface. In discretized form, the equations of motion for the substructure are written as

$$\mathbf{M}\ddot{\mathbf{u}} + \mathbf{K}\mathbf{u} + \mathbf{f}_{\mathrm{N}} = \mathbf{f}_{\mathrm{ext}} \tag{1}$$

where $\mathbf{M}$ and $\mathbf{K}$ are respectively the mass and stiffness matrices, $\mathbf{u}$ is the relative displacement vector, $\mathbf{f}_{\mathrm{N}}$ is the vector of displacement-dependent normal contact forces (discussed in Section 2.3), and $\mathbf{f}_{\mathrm{ext}}$is the externally applied loading vector. The matrices are *n* x *n* and the vectors are *n* x 1. Each dot placed over $\mathbf{u}$ represents its derivative with respect to time. These equations can be partitioned into interior *i* and interface *b* DOF as

$$\begin{bmatrix} \mathbf{M}_{\mathrm{ii}} & \mathbf{M}_{\mathrm{ib}} \\ \mathbf{M}_{\mathrm{bi}} & \mathbf{M}_{\mathrm{bb}} \end{bmatrix} \begin{Bmatrix} \ddot{\mathbf{u}}_{\mathrm{i}} \\ \ddot{\mathbf{u}}_{\mathrm{b}} \end{Bmatrix} + \begin{bmatrix} \mathbf{K}_{\mathrm{ii}} & \mathbf{K}_{\mathrm{ib}} \\ \mathbf{K}_{\mathrm{bi}} & \mathbf{K}_{\mathrm{bb}} \end{bmatrix} \begin{Bmatrix} \mathbf{u}_{\mathrm{i}} \\ \mathbf{u}_{\mathrm{b}} \end{Bmatrix} + \begin{Bmatrix} \mathbf{0} \\ \mathbf{f}_{\mathrm{N,b}} \end{Bmatrix} = \begin{Bmatrix} \mathbf{f}_{\mathrm{ext,i}} \\ \mathbf{f}_{\mathrm{ext,b}} \end{Bmatrix} \tag{2}$$

The mass and stiffness from the interior degrees of freedom are used to form the fixed-interface (FI) modes of the system through a partitioned eigenanalysis, i.e.

$$[\mathbf{K}_{\mathrm{ii}} - (\omega_{\mathrm{s}}^{\mathrm{FI}})^2 \mathbf{M}_{\mathrm{ii}}]\boldsymbol{\varphi}_{\mathrm{s}}^{\mathrm{FI}} = \mathbf{0} \tag{3}$$

The eigenvectors $\boldsymbol{\varphi}_{\mathrm{s}}^{\mathrm{FI}}$ (s = 1, 2, …, $\mathrm{n_{FI}}$) form the FI modal matrix

$$\boldsymbol{\Phi}^{\mathrm{FI}} = \begin{bmatrix} \boldsymbol{\varphi}_1^{\mathrm{FI}} & \boldsymbol{\varphi}_2^{\mathrm{FI}} & \cdots & \boldsymbol{\varphi}_{\mathrm{n_{FI}}}^{\mathrm{FI}} \end{bmatrix} \tag{4}$$

where $\mathrm{n_{FI}}$ is an integer much smaller than the original number of DOF in set *i*. The truncation of modes in this step introduces the model reduction desired by the HCB process. The eigenshapes are combined with a set of static constraint modes that describe how the interior DOF respond when each interface DOF is moved independently. This is defined by the static condensation

$$\boldsymbol{\Psi}^{\mathrm{HCB}} = -\mathbf{K}_{\mathrm{ii}}^{-1}\mathbf{K}_{\mathrm{ib}} \tag{5}$$

The combination of FI modes and constraint modes form a basis for the interior DOF of the substructure, and are arranged to form the HCB transformation matrix as

$$\mathbf{T}^{\mathrm{HCB}} = \begin{bmatrix} \boldsymbol{\Phi}^{\mathrm{FI}} & \boldsymbol{\Psi}^{\mathrm{HCB}} \\ \mathbf{0} & \mathbf{I} \end{bmatrix} \tag{6}$$

which converts the interior DOF of the substructure to generalized HCB coordinates through the transformation

$$\mathbf{u} = \mathbf{T}^{\mathrm{HCB}}\mathbf{v} \tag{7a}$$

$$\begin{Bmatrix} \mathbf{u}_{\mathrm{i}} \\ \mathbf{u}_{\mathrm{b}} \end{Bmatrix} = \begin{bmatrix} \boldsymbol{\Phi}^{\mathrm{FI}} & \boldsymbol{\Psi}^{\mathrm{HCB}} \\ \mathbf{0} & \mathbf{I} \end{bmatrix} \begin{Bmatrix} \mathbf{q}_{\mathrm{i}} \\ \mathbf{u}_{\mathrm{b}} \end{Bmatrix} \tag{7b}$$

The vector $\mathbf{v}$ is the HCB generalized coordinate and $\mathbf{q}_{\mathrm{i}}$ is the modal representation of the interior partition of the substructure. The reduced mass and stiffness matrices, as well as the reduced load vectors, are computed via

$$\mathbf{M}^{\mathrm{HCB}} = (\mathbf{T}^{\mathrm{HCB}})^{\mathrm{T}}\mathbf{M}\mathbf{T}^{\mathrm{HCB}}, \qquad \mathbf{K}^{\mathrm{HCB}} = (\mathbf{T}^{\mathrm{HCB}})^{\mathrm{T}}\mathbf{K}\mathbf{T}^{\mathrm{HCB}}$$
$$\mathbf{f}_{\mathrm{N}}^{\mathrm{HCB}} = (\mathbf{T}^{\mathrm{HCB}})^{\mathrm{T}}\mathbf{f}_{\mathrm{N}}, \qquad \mathbf{f}_{\mathrm{ext}}^{\mathrm{HCB}} = (\mathbf{T}^{\mathrm{HCB}})^{\mathrm{T}}\mathbf{f}_{\mathrm{ext}} \tag{8}$$

where $^{\mathrm{T}}$ is the transpose operator. The dimension of the problem after HCB reduction is $n_{FI} + n_b$, where n_{FI} is the number of retained fixed-interface modes, and n_b is the total number of interface DOF. The equations of motion for a substructure in HCB coordinates are

$$\mathbf{M}^{\mathrm{HCB}}\ddot{\mathbf{v}} + \mathbf{K}^{\mathrm{HCB}}\mathbf{v} + \mathbf{f}_{\mathrm{N}}^{\mathrm{HCB}} = \mathbf{f}_{\mathrm{ext}}^{\mathrm{HCB}} \tag{9a}$$

$$\begin{bmatrix} \mathbf{I}_{\mathrm{ii}} & \mathbf{M}_{\mathrm{ib}}^{\mathrm{HCB}} \\ \mathbf{M}_{\mathrm{bi}}^{\mathrm{HCB}} & \mathbf{M}_{\mathrm{bb}}^{\mathrm{HCB}} \end{bmatrix} \begin{Bmatrix} \ddot{\mathbf{q}}_{\mathrm{i}} \\ \ddot{\mathbf{u}}_{\mathrm{b}} \end{Bmatrix} + \begin{bmatrix} \mathbf{\Lambda}_{\mathrm{ii}}^{\mathrm{FI}} & \mathbf{0} \\ \mathbf{0} & \mathbf{K}_{\mathrm{bb}}^{\mathrm{HCB}} \end{bmatrix} \begin{Bmatrix} \mathbf{q}_{\mathrm{i}} \\ \mathbf{u}_{\mathrm{b}} \end{Bmatrix} + \begin{Bmatrix} \mathbf{0} \\ \mathbf{f}_{\mathrm{N,b}}^{\mathrm{HCB}} \end{Bmatrix} = \begin{Bmatrix} \mathbf{f}_{\mathrm{ext,i}}^{\mathrm{HCB}} \\ \mathbf{f}_{\mathrm{ext,b}}^{\mathrm{HCB}} \end{Bmatrix} \tag{9b}$$

where $\mathbf{I}_{\mathrm{ii}}$ and $\mathbf{\Lambda}_{\mathrm{ii}}^{\mathrm{FI}}$ are the identity matrix and diagonal matrix of fixed-interface eigenvalues, respectively. This form arises from the orthogonality properties of the modal matrix $\mathbf{\Phi}^{\mathrm{FI}}$ in the HCB coordinate transformation.

2.2. Interface Modal Basis

Any interface reduction basis must satisfy a number of criteria: (1) allow for realistic deformations in the contact area, (2) reproduce the distribution of contact forces, (3) match the overall dynamic response of the HCB model within a reasonable margin of error, and (4) be efficient enough to provide overall computational savings. This research attempts to meet each of these criteria by utilizing an interface reduction technique that is a modification of the system-level characteristic constraint modes [9,10]. In addition to these mode shapes, the basis is augmented with the static deformation shape obtained from a nonlinear static preload analysis, as it is inefficient to resolve the interface kinematics with dynamic modes alone.

2.2.1 Extended System-Level Characteristic Constraint Modes About Preloaded State

The traditional method of system-level characteristic constraint modes, or SCC method, transforms all physical interface DOF in the HCB model into truncated modal DOF, such that the resulting model is defined entirely in the modal domain. In some cases, it is desirable to retain some portion of the interface as physical DOF. For example, it may be necessary to retain physical DOF when loads are applied near substructure boundaries (e.g. bolt preload force). A novel method to achieve this is introduced here, and referred to as the extended system-level characteristic constraint mode method, or SCCe method.

To reduce some of the interface DOF to modal DOF, and retain the rest as physical DOF, a given substructure must now be partitioned into three sets: the interior DOF *i* (i.e. fixed-interface mode partition), physical interface DOF *p*, and reduced interface DOF *r*. The HCB system mass and stiffness matrices, according to these partitions, are

$$\mathbf{M}^{\mathrm{HCB}} = \begin{bmatrix} \mathbf{I}_{\mathrm{ii}} & \mathbf{M}_{\mathrm{ir}}^{\mathrm{HCB}} & \mathbf{M}_{\mathrm{ip}}^{\mathrm{HCB}} \\ \mathbf{M}_{\mathrm{ri}}^{\mathrm{HCB}} & \mathbf{M}_{\mathrm{rr}}^{\mathrm{HCB}} & \mathbf{M}_{\mathrm{rp}}^{\mathrm{HCB}} \\ \mathbf{M}_{\mathrm{pi}}^{\mathrm{HCB}} & \mathbf{M}_{\mathrm{pr}}^{\mathrm{HCB}} & \mathbf{M}_{\mathrm{pp}}^{\mathrm{HCB}} \end{bmatrix}, \qquad \mathbf{K}^{\mathrm{HCB}} = \begin{bmatrix} \mathbf{\Lambda}_{\mathrm{ii}}^{\mathrm{FI}} & \mathbf{0} & \mathbf{0} \\ \mathbf{0} & \mathbf{K}_{\mathrm{rr}}^{\mathrm{HCB}} & \mathbf{K}_{\mathrm{rp}}^{\mathrm{HCB}} \\ \mathbf{0} & \mathbf{K}_{\mathrm{pr}}^{\mathrm{HCB}} & \mathbf{K}_{\mathrm{pp}}^{\mathrm{HCB}} \end{bmatrix} \tag{10}$$

The contact state of the model about its preloaded state is important to capturing the correct dynamic response, and hence the SCCe modal basis must account for this. This is achieved by linearizing the preloaded HCB model to include stiffness contributions from the contact areas that form upon fastening/preloading substructures coming into contact. The static deformation due to the preload force (denoted as $\mathbf{v}^{\mathrm{e}}$ in HCB coordinates) is solved using a nonlinear static

solver (see Section 2.2.2). A linearized stiffness matrix (denoted with *–c* due to the added constraints) is formed by summing the linear HCB stiffness matrix and the Jacobian of the normal contact force, evaluated about the deformed state,

$$\mathbf{K}^{\mathrm{HCB-c}} = \mathbf{K}^{\mathrm{HCB}} + \left[\frac{\partial \mathbf{f}_{\mathrm{N}}^{\mathrm{HCB}}}{\partial \mathbf{v}}\right]_{\mathbf{v}=\mathbf{v}^{\mathrm{e}}}$$

A set of SCCe mode shapes is computed from a second partitioned eigenanalysis, employing the linearized stiffness matrix and isolating the reduced interface DOF *r*

$$[\mathbf{K}_{\mathrm{rr}}^{\mathrm{HCB-c}} - (\omega^{\mathrm{SCCe-c}})^2 \mathbf{M}_{\mathrm{rr}}^{\mathrm{HCB}}]\boldsymbol{\varphi}_{\mathrm{s}}^{\mathrm{SCCe-c}} = \mathbf{0} \tag{12}$$

A limited set of eigenvectors $\boldsymbol{\varphi}_{\mathrm{s}}^{\mathrm{SCCe-c}} = (\mathrm{s} = 1, 2, \ldots, \mathrm{n_S})$ are assembled into the columns of the constrained SCCe modal matrix

$$\boldsymbol{\Phi}^{\mathrm{SCCe-c}} = \left[\boldsymbol{\varphi}_1^{\mathrm{SCCe-c}} \quad \boldsymbol{\varphi}_2^{\mathrm{SCCe-c}} \quad \cdots \quad \boldsymbol{\varphi}_{\mathrm{n_s}}^{\mathrm{SCCe-c}}\right] \tag{13}$$

where $\mathrm{n_S}$ is a number smaller than the original number of DOF in set *r*.

The modes contained in $\boldsymbol{\Phi}^{\mathrm{SCCe-c}}$ provide a good representation of the local interface dynamics when the interface is in contact due to the additional term in the contact stiffness, $\mathbf{K}^{\mathrm{HCB-c}}$. If the interface loses contact during a vibration response, then these modes may be insufficient. In order to address this, the eigenanalysis can be repeated using the original stiffness matrix $\mathbf{K}^{\mathrm{HCB}}$, such that a new set of *unconstrained* modes (denoted with *–u*) can be added to the reduction basis.

$$[\mathbf{K}_{\mathrm{rr}}^{\mathrm{HCB}} - (\omega^{\mathrm{SCCe-u}})^2 \mathbf{M}_{\mathrm{rr}}^{\mathrm{HCB}}]\boldsymbol{\varphi}_{\mathrm{s}}^{\mathrm{SCCe-u}} = \mathbf{0} \tag{14}$$

The first $\mathrm{n_S}$ unconstrained eigenvectors are used to build the unconstrained SCCe modal matrix as

$$\boldsymbol{\Phi}^{\mathrm{SCCe-u}} = \left[\boldsymbol{\varphi}_1^{\mathrm{SCCe-u}} \quad \boldsymbol{\varphi}_2^{\mathrm{SCCe-u}} \quad \cdots \quad \boldsymbol{\varphi}_{\mathrm{n_s}}^{\mathrm{SCCe-u}}\right] \tag{15}$$

Both sets of eigenmodes described in Eqs. (13) and (15) use the *r*-*r* partition of the system matrices, so they inherently fix the motion of the physical interface DOF (set *p*) to be zero. To alleviate this issue, static constraint modes are added to the interface reduction set, similar to those in original the HCB method

$$\boldsymbol{\Psi}^{\mathbf{SCCe}} = -(\mathbf{K}_{\mathrm{rr}}^{\mathrm{HCB-c}})^{-1}\mathbf{K}_{\mathrm{rp}}^{\mathrm{HCB-c}} \tag{16}$$

Combining the dual set of eigenmodes with the constraint modes, along with appropriately-sized zero and identity partitions, the SCCe transformation matrix is formed as

$$\mathbf{T}^{\mathrm{SCCe}} = \begin{bmatrix} \mathbf{I} & \mathbf{0} & \mathbf{0} & \mathbf{0} \\ \mathbf{0} & \boldsymbol{\Phi}^{\mathrm{SCCe-c}} & \boldsymbol{\Phi}^{\mathrm{SCCe-u}} & \boldsymbol{\Psi}^{\mathbf{SCCe}} \\ \mathbf{0} & \mathbf{0} & \mathbf{0} & \mathbf{I} \end{bmatrix} \tag{17}$$

This transformation uses a combination of dynamic ($\boldsymbol{\Phi}^{\mathrm{SCCe-c}}, \boldsymbol{\Phi}^{\mathrm{SCCe-u}}$) and static ($\boldsymbol{\Psi}^{\mathbf{SCCe}}$) shapes to convert the *r* portion of the model to modal DOF, while retaining the *p* portion as physical DOF. The transformation between HCB coordinates and SCCe coordinates becomes

$$\mathbf{v} = \mathbf{T}^{\mathrm{SCCe}}\mathbf{w} \tag{18a}$$

$$\begin{Bmatrix}\mathbf{q}_i\\ \mathbf{u}_r\\ \mathbf{u}_p\end{Bmatrix}=\begin{bmatrix}\mathbf{I} & \mathbf{0} & \mathbf{0} & \mathbf{0}\\ \mathbf{0} & \boldsymbol{\Phi}^{\mathrm{SCCe-c}} & \boldsymbol{\Phi}^{\mathrm{SCCe-u}} & \boldsymbol{\Psi}^{\mathbf{SCCe}}\\ \mathbf{0} & \mathbf{0} & \mathbf{0} & \mathbf{I}\end{bmatrix}\begin{Bmatrix}\mathbf{q}_i\\ \mathbf{q}_c\\ \mathbf{q}_u\\ \mathbf{u}_p\end{Bmatrix} \tag{18b}$$

where $\mathbf{w}$ is the SCCe generalized coordinate vector, and $\mathbf{q}_c$ and $\mathbf{q}_u$ are the constrained and unconstrained modal DOF in the *r* partition, respectively.

2.2.2 Static Preload Deformation

The inclusion of the static preload shape $\mathbf{v}^e$ in the reduction basis ensures that the SCCe model is exact for the initial preload analysis performed on the nonlinear HCB model in Eqs. (9a) and (9b). This shape is determined by solving the following equations for static equilibrium, stated in HCB coordinates

$$\mathbf{K}^{\mathrm{HCB}}\mathbf{v}^e+\mathbf{f}_N^{\mathrm{HCB}}=\mathbf{b}^e\mathrm{f}^e \tag{19}$$

where $\mathbf{b}^e$ is a mapping vector that positions and orients the scalar preload force amplitude f^e at the correct physical DOF. In partitioned form, the equations are

$$\begin{bmatrix}\boldsymbol{\Lambda}_{ii}^{\mathrm{FI}} & \mathbf{0} & \mathbf{0}\\ \mathbf{0} & \mathbf{K}_{rr}^{\mathrm{HCB}} & \mathbf{K}_{rp}^{\mathrm{HCB}}\\ \mathbf{0} & \mathbf{K}_{pr}^{\mathrm{HCB}} & \mathbf{K}_{pp}^{\mathrm{HCB}}\end{bmatrix}\begin{Bmatrix}\mathbf{q}_i^e\\ \mathbf{u}_r^e\\ \mathbf{u}_p^e\end{Bmatrix}+\begin{Bmatrix}\mathbf{0}\\ \mathbf{f}_{N,r}^{\mathrm{HCB}}\\ \mathbf{f}_{N,p}^{\mathrm{HCB}}\end{Bmatrix}=\begin{Bmatrix}\mathbf{0}\\ \mathbf{0}\\ \mathbf{b}_p^e\mathrm{f}^e\end{Bmatrix} \tag{20}$$

Due to the nonlinearity introduced by the contact force $\mathbf{f}_N^{\mathrm{HCB}}$, the displacement vector $\mathbf{v}^e=[\mathbf{q}_i^e \quad \mathbf{u}_r^e \quad \mathbf{u}_p^e]^{\mathrm{T}}$ must be determined using an iterative solver. In this research, a damped Newton Raphson method was employed.

2.2.3. Total SCCe Transformation Matrix

The static deformation vector is concatenated at the end of $\mathbf{T}^{\mathrm{SCCe}}$ to build the final SCCe transformation matrix $\mathbf{T}^{\mathrm{SCCe+}}$

$$\mathbf{T}^{\mathrm{SCCe+}}=[\mathbf{T}^{\mathrm{SCCe}} \quad \mathbf{v}^e] \tag{21a}$$

$$\mathbf{T}^{\mathrm{SCCe+}}=\begin{bmatrix}\mathbf{I} & \mathbf{0} & \mathbf{0} & \mathbf{0} & \mathbf{q}_i^e\\ \mathbf{0} & \boldsymbol{\Phi}^{\mathrm{SCCe-c}} & \boldsymbol{\Phi}^{\mathrm{SCCe-u}} & \boldsymbol{\Psi}^{\mathbf{SCCe}} & \mathbf{u}_r^e\\ \mathbf{0} & \mathbf{0} & \mathbf{0} & \mathbf{I} & \mathbf{u}_p^e\end{bmatrix} \tag{21b}$$

This matrix performs the same transformation as Eqs. (18a) and (18b), but adds one more DOF from the preload vector. The HCB coordinate $\mathbf{v}$ is transformed to the new SCCe coordinates $\mathbf{w}^+$ via

$$\mathbf{v}=\mathbf{T}^{\mathrm{SCCe+}}\mathbf{w}^+ \tag{22a}$$

$$\begin{Bmatrix}\mathbf{q}_i\\ \mathbf{u}_r\\ \mathbf{u}_p\end{Bmatrix}=\begin{bmatrix}\mathbf{I} & \mathbf{0} & \mathbf{0} & \mathbf{0} & \mathbf{q}_i^e\\ \mathbf{0} & \boldsymbol{\Phi}^{\mathrm{SCCe-c}} & \boldsymbol{\Phi}^{\mathrm{SCCe-u}} & \boldsymbol{\Psi}^{\mathbf{SCCe}} & \mathbf{u}_r^e\\ \mathbf{0} & \mathbf{0} & \mathbf{0} & \mathbf{I} & \mathbf{u}_p^e\end{bmatrix}\begin{Bmatrix}\mathbf{q}_i\\ \mathbf{q}_c\\ \mathbf{q}_u\\ \mathbf{u}_p\\ \mathrm{q}_e\end{Bmatrix} \tag{22b}$$

where q_e is the scalar DOF introduced by the inclusion of $\mathbf{v}^e$.

The variety of shapes that make up $\mathbf{T}^{\mathrm{SCCe+}}$ can lead to a basis set that is not necessarily linearly independent. The singular value decomposition (SVD) reforms $\mathbf{T}^{\mathrm{SCCe+}}$ as

$$\mathbf{T}^{\mathrm{SCCe+}} = \mathbf{U}^{\mathrm{SCCe+}}\mathbf{\Sigma}^{\mathrm{SCCe+}}\mathbf{V}^{\mathrm{SCCe+}} \tag{23}$$

where $\mathbf{U}^{\mathrm{SCCe+}}$ and $\mathbf{V}^{\mathrm{SCCe+}}$ are the left and right singular vectors, respectively, and $\mathbf{\Sigma}^{\mathrm{SCCe+}}$ is a diagonal matrix of singular values. The vectors in $\mathbf{U}^{\mathrm{SCCe+}}$ form an orthonormal basis for the column space of $\mathbf{T}^{\mathrm{SCCe+}}$, so they are taken as the final transformation matrix to convert between HCB and SCCe coordinates. Thus, the SCCe system matrices and load vectors are computed as

$$\begin{gathered}\mathbf{M}^{\mathrm{SCCe}} = (\mathbf{U}^{\mathrm{SCCe+}})^{\mathrm{T}}\mathbf{M}^{\mathrm{HCB}}\mathbf{U}^{\mathrm{SCCe+}}, \qquad \mathbf{K}^{\mathrm{SCCe}} = (\mathbf{U}^{\mathrm{SCCe+}})^{\mathrm{T}}\mathbf{K}\mathbf{U}^{\mathrm{SCCe+}} \\ \mathbf{f}_{\mathrm{N}}^{\mathrm{SCCe}} = (\mathbf{U}^{\mathrm{SCCe+}})^{\mathrm{T}}\mathbf{f}_{\mathrm{N}}^{\mathrm{HCB}}, \qquad \mathbf{f}_{\mathrm{ext}}^{\mathrm{SCCe}} = (\mathbf{U}^{\mathrm{SCCe+}})^{\mathrm{T}}\mathbf{f}_{\mathrm{ext}}^{\mathrm{HCB}}\end{gathered} \tag{24}$$

The dimension of the problem is now $n_{FI} + 2n_S + n_p + 1$, where n_{FI} is the number of retained fixed-interface modes, n_S is the number of retained SCCe modes (one set of constrained, one set of unconstrained), n_p is the number of physical interface DOF, and the 1 accounts for the static preload shape.

The equations of motion for the system in SCCe coordinates are

$$\mathbf{M}^{\mathrm{SCCe}}\ddot{\mathbf{w}}^{+} + \mathbf{K}^{\mathrm{SCCe}}\mathbf{w}^{+} + \mathbf{f}_{\mathrm{N}}^{\mathrm{SCCe}} = \mathbf{f}_{\mathrm{ext}}^{\mathrm{SCCe}} \tag{25a}$$

$$\begin{bmatrix} \mathbf{I}_{\mathrm{ii}} & \mathbf{M}_{\mathrm{ic}}^{\mathrm{SCCe}} & \mathbf{M}_{\mathrm{iu}}^{\mathrm{SCCe}} & \mathbf{M}_{\mathrm{ip}}^{\mathrm{SCCe}} & \mathbf{M}_{\mathrm{ie}}^{\mathrm{SCCe}} \\ \mathbf{M}_{\mathrm{ci}}^{\mathrm{SCCe}} & \mathbf{M}_{\mathrm{cc}}^{\mathrm{SCCe}} & \mathbf{M}_{\mathrm{cu}}^{\mathrm{SCCe}} & \mathbf{M}_{\mathrm{cp}}^{\mathrm{SCCe}} & \mathbf{M}_{\mathrm{ce}}^{\mathrm{SCCe}} \\ \mathbf{M}_{\mathrm{ui}}^{\mathrm{SCCe}} & \mathbf{M}_{\mathrm{uc}}^{\mathrm{SCCe}} & \mathbf{M}_{\mathrm{uu}}^{\mathrm{SCCe}} & \mathbf{M}_{\mathrm{up}}^{\mathrm{SCCe}} & \mathbf{M}_{\mathrm{ue}}^{\mathrm{SCCe}} \\ \mathbf{M}_{\mathrm{pi}}^{\mathrm{SCCe}} & \mathbf{M}_{\mathrm{pc}}^{\mathrm{SCCe}} & \mathbf{M}_{\mathrm{pu}}^{\mathrm{SCCe}} & \mathbf{M}_{\mathrm{pp}}^{\mathrm{SCCe}} & \mathbf{M}_{\mathrm{pe}}^{\mathrm{SCCe}} \\ \mathbf{M}_{\mathrm{ei}}^{\mathrm{SCCe}} & \mathbf{M}_{\mathrm{ec}}^{\mathrm{SCCe}} & \mathbf{M}_{\mathrm{eu}}^{\mathrm{SCCe}} & \mathbf{M}_{\mathrm{ep}}^{\mathrm{SCCe}} & \mathbf{M}_{\mathrm{ee}}^{\mathrm{SCCe}} \end{bmatrix} \begin{Bmatrix} \ddot{\mathbf{q}}_{\mathrm{i}} \\ \ddot{\mathbf{q}}_{\mathrm{c}} \\ \ddot{\mathbf{q}}_{\mathrm{u}} \\ \ddot{\mathbf{u}}_{\mathrm{p}} \\ \ddot{\mathrm{q}}_{\mathrm{e}} \end{Bmatrix} + \begin{bmatrix} \mathbf{\Lambda}_{\mathrm{ii}}^{\mathrm{FI}} & \mathbf{0} & \mathbf{0} & \mathbf{0} & \mathbf{0} \\ \mathbf{0} & \mathbf{K}_{\mathrm{cc}}^{\mathrm{SCCe}} & \mathbf{K}_{\mathrm{cu}}^{\mathrm{SCCe}} & \mathbf{K}_{\mathrm{cp}}^{\mathrm{SCCe}} & \mathbf{K}_{\mathrm{ce}}^{\mathrm{SCCe}} \\ \mathbf{0} & \mathbf{K}_{\mathrm{uc}}^{\mathrm{SCCe}} & \mathbf{K}_{\mathrm{uu}}^{\mathrm{SCCe}} & \mathbf{K}_{\mathrm{up}}^{\mathrm{SCCe}} & \mathbf{K}_{\mathrm{ue}}^{\mathrm{SCCe}} \\ \mathbf{0} & \mathbf{K}_{\mathrm{pc}}^{\mathrm{SCCe}} & \mathbf{K}_{\mathrm{pu}}^{\mathrm{SCCe}} & \mathbf{K}_{\mathrm{pp}}^{\mathrm{SCCe}} & \mathbf{K}_{\mathrm{pe}}^{\mathrm{SCCe}} \\ \mathbf{0} & \mathbf{K}_{\mathrm{ec}}^{\mathrm{SCCe}} & \mathbf{K}_{\mathrm{eu}}^{\mathrm{SCCe}} & \mathbf{K}_{\mathrm{ep}}^{\mathrm{SCCe}} & \mathbf{K}_{\mathrm{ee}}^{\mathrm{SCCe}} \end{bmatrix} \begin{Bmatrix} \mathbf{q}_{\mathrm{i}} \\ \mathbf{q}_{\mathrm{c}} \\ \mathbf{q}_{\mathrm{u}} \\ \mathbf{u}_{\mathrm{p}} \\ \mathrm{q}_{\mathrm{e}} \end{Bmatrix} + \begin{Bmatrix} \mathbf{0} \\ \mathbf{f}_{\mathrm{N,c}}^{\mathrm{SCCe}} \\ \mathbf{f}_{\mathrm{N,u}}^{\mathrm{SCCe}} \\ \mathbf{f}_{\mathrm{N,p}}^{\mathrm{SCCe}} \\ \mathbf{f}_{\mathrm{N,e}}^{\mathrm{SCCe}} \end{Bmatrix} = \begin{Bmatrix} \mathbf{f}_{\mathrm{ext,i}}^{\mathrm{SCCe}} \\ \mathbf{f}_{\mathrm{ext,c}}^{\mathrm{SCCe}} \\ \mathbf{f}_{\mathrm{ext,u}}^{\mathrm{SCCe}} \\ \mathbf{f}_{\mathrm{ext,p}}^{\mathrm{SCCe}} \\ \mathbf{f}_{\mathrm{ext,e}}^{\mathrm{SCCe}} \end{Bmatrix} \tag{25b}$$

Note that, although the normal contact force vector $\mathbf{f}_{\mathrm{N}}^{\mathrm{SCCe}}$ has been reduced to SCCe coordinates, it must still be computed in HCB coordinates, where all interface DOF are physically represented. In nonlinear dynamic simulations, this requires a transformation from SCCe to HCB coordinates at every time step to evaluate the nonlinear forces. The advantage that comes from this reduction is twofold: (1) the size of the equations to solve is smaller compared to the HCB model and (2) the high frequency content has been truncated and thus improves the critical time step in explicit solvers.

2.3. Normal Contact Model

Contact in the normal direction is modeled using a node-to-node approach with the penalty method [11]. In this method, the normal gap *g* between a contacting node pair can be either negative (in contact) or positive (out of contact). For a particular node pair *j*, the normal gap is

$$\mathrm{g}^{\mathrm{j}} = \left(\mathrm{Y}_1^{\mathrm{j}} + \Delta\mathrm{Y}_1^{\mathrm{j}}\right) - \left(\mathrm{Y}_2^{\mathrm{j}} + \Delta\mathrm{Y}_2^{\mathrm{j}}\right) \tag{26}$$

where the Y's are the undeformed normal coordinates, and the ΔY's are the physical relative displacements in the normal direction. The subscripts 1 and 2 refer to the two nodes in node pair *j*. The penalty method states that the normal contact force at node *j* $\mathrm{f}_{\mathrm{N}}^{\mathrm{j}}$ can be written as

$$f_N^j = \begin{cases} k_{pen} g^j, & g^j < 0 \\ 0 \quad , & g^j \geq 0 \end{cases} \tag{27}$$

where k_{pen} is the penalty stiffness value. This defines the penalty force as proportional to the gap when the nodes are in contact ($g^j < 0$), and zero when the nodes are out of contact ($g^j \geq 0$). The node-to-node contact model assumes that relative tangential displacements are small, and thus node pairs do not change during dynamic simulation. Construction of the normal contact force vector $\mathbf{f}_N$ is a matter of positioning and orienting each nodal force f_N^j using a corresponding mapping vector $\mathbf{b}_N^j$ as

$$\mathbf{f}_N = \sum_{j=1}^{n_n} \mathbf{b}_N^j f_N^j \tag{28}$$

where n_n is the number of node pairs all interfaces of the system.

2.4 Time Integration Schemes

The response time histories of the reduced order models are computed using one of two different 2nd order accurate methods: an explicit scheme from Chung and Lee [12], and the implicit Hilber-Hughes-Taylor α (HHT- α) method extended to nonlinear systems [13]. The implicit method is implemented with $\alpha = 0$, yielding the constant average acceleration method, which is unconditionally stable for linear systems. The Chung-Lee scheme is conditionally stable, with a critical time step requirement that is dependent on its single free parameter, β_{CL},

$$\Delta t_{cr} = \frac{2}{\omega_{max}\sqrt{4\beta_{CL} - 3}} \tag{29}$$

where Δt_{cr} is the critical time step length, and ω_{max} is the largest natural circular frequency in the system. The Chung-Lee parameter β_{CL} is chosen to be 28/27, the maximum permissible value in the stability limit of $1 \leq \beta_{CL} \leq 28/27$. This selection improves stability by introducing slight numerical dissipation of high-frequency responses, which mitigates the amplification of numerical errors.

3. Numerical Studies: Two-Beam Assembly with Frictionless Contact

3.1. Model Description

Figure 1a shows the benchmark finite element model under consideration, which consists of two identical C-beams bolted together at each end. Each individual C-beam is 50.8 cm long, 3.2 cm wide, 1.27 cm thick at its ends, and 0.95 cm thick at the mid-section. A total of 24,944 first order hexahedral elements are used to model each individual C-beam, and they are made of linear elastic structural steel. Table 1 provides a summary of material properties used for the C-beams.

These are connected by 5/16-inch diameter steel bolts at each end that are modeled with 25 discretized beam elements along the y-axis, as depicted in Figure 1b. The bolt ends are connected rigidly to a circular patch of nodes on the C-beams to represent clamping boundary conditions through a nut-washer-bolt assembly. The C-beam assembly has simply supported boundary conditions at all DOF along the z-directional line on the lower beam ends. The full fidelity finite element model has a total of 94,244 physical DOF.

The model has two areas where the C-beams come into contact; each is 3.2 cm wide by 5.0 cm long, as indicated in Figure 1b). The interface surfaces are meshed in such a way that their nodal locations are coincident and unmerged in the undeformed state, allowing for direct implementation of node-to-node contact elements. The Hurty/Craig-Bampton model is defined such that the boundary DOF include the nodes along these interface surfaces and the four nodes at each end of the beam elements (to apply the preload force); the remaining DOF are partitioned to interior DOF. Three different reduced order models are generated with fixed-interface mode frequencies cut off at 2 kHz, 3 kHz, and 4 kHz. The DOF count in the reduced model is dominated by the 3,660 boundary DOF that account for the contacting surfaces, while 24 DOF pertain to the bolt DOF and 8 to 16 DOF for the fixed-interface modes, depending on the cutoff frequency (see Section 3.3). The HCB reduction is performed using the Sierra Structural Dynamics (Sierra/SD) [14] finite element code developed at Sandia National Laboratories.

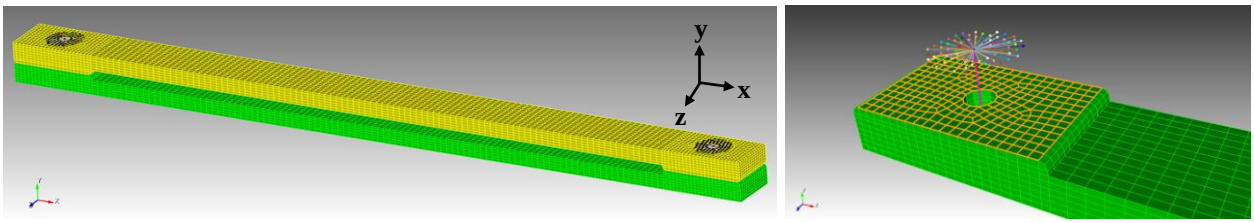

(a) (b)

Figure 1. (a) Finite element model of bolted C-beam assembly with coordinate axes. (b) Close-up view of interface surface with bolt DOF spider.

Contact at the interface surfaces is considered through node-to-node penalty elements in the normal direction [11]. Selection of the penalty stiffness k_{pen} is critical in the accuracy and stability of the penalty method - using a stiffness value that is too small allows excessive and non-physical nodal interpenetration, while a value that is too high can cause numerical ill-conditioning or instability. Preliminary studies indicated that a value of 3.78×10^9 N/m was sufficient to avoid excessive node overlap, while retaining stability and convergence.

Table 1. Summary of material properties used in finite element model of C-beams.

Symbol	Description	Numerical Value	
E	Young's modulus	194	GPa
ν	Poisson's ratio	0.290	
ρ	Mass density	8000	kg/m^3

3.2. Static Preloading of Bolt Elements

A static preload force f^e is applied to the ends of the bolt elements, to simulate the effect of bolt torque clamping the C-beams together. The preload force is obtained via an artificial strain ε_{art}, which leads to the following expression.

$$f^e = EA\varepsilon_{art} \tag{30}$$

The cross-sectional area A of each bolt is 4.95 x 10^{-5} m^2, and the Young's modulus E is the same as that of the C-beams (194 GPa). To ensure that a physically reasonable preload force is applied, a target internal bolt force is obtained using the DIN 946 standard [15] equation to convert applied torque T to transmitted axial force f_{tr}.

$$f_{tr} = \frac{T}{0.159P + 0.578d\mu_T + 0.5D_f\mu_H} \tag{31}$$

where P is the bolt thread pitch, d is the nominal bolt diameter, D_f is the effective diameter in contact, μ_T is the thread friction coefficient, and μ_H is the head friction coefficient. Inputs for these variables are summarized in Table 2. For a typical applied torque of 18.5 ft-lb (25.1 N-m), the transmitted axial force is computed as 2.91 kN.

The correct ε_{art} (and therefore f^e) is obtained through an iterative procedure that incrementally alters ε_{art}, and applies the corresponding f^e, until the resulting internal bolt axial force matches the theoretical transmitted force f_{tr}. This procedure indicates that an artificial strain of $3.32 \cdot 10^{-4}$ (corresponding to a preload force of 3.19 kN) is appropriate to produce an internal axial force equal to 2.91 kN.

Table 2. Summary of bolt preload parameters.

Symbol	Description	Numerical Value	
T	Applied bolt torque	25.1	N-m
P	Bolt thread pitch	0.00106	m
d	Nominal bolt diameter	0.00794	m
D_f	Effective diameter in contact	0.0191	m
μ_T	Thread friction coefficient	0.600	
μ_H	Head friction coefficient	0.600	
f_{tr}	Transmitted axial force	2.91	kN
ε_{art}	Artificial preload strain	3.32E-04	
f^e	Preload force	3.19	kN

A visualization of the preloaded deformation mapped to the full-field model is displayed in Figure 2, along with a close-up view of the interface, showing how the preload force indents the C-beam surfaces and causes receding of the contact area.

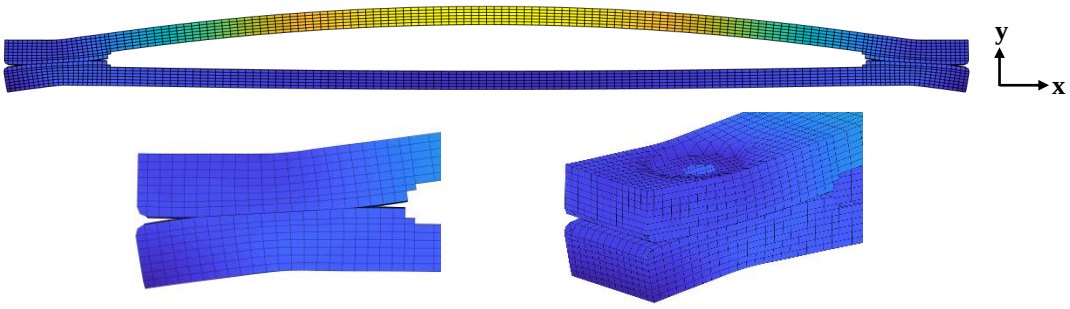

Figure 2. Amplified deformation after static preload, with close-up view of interface.

3.3. Results: Full-interface Model

A critical step in the Hurty/Craig-Bampton (HCB) reduction is determining the number of fixed-interface (FI) modes to retain, which is established by discarding FI modes with frequencies above a defined threshold. For a given loading bandwidth and pattern, the dynamic response of the system will converge to the "true" solution by increasing the frequency cut-off limit. The number of FI modes required for convergence is considered adequate to capture the important dynamic characteristics of the system. For this research, so-called "cutoff" frequencies of 2kHz, 3kHz, and 4kHz are examined and summarized in Table 3. The lowest fixed-interface mode frequency in all cases is 288 Hz.

Critical time step lengths are computed for the Chung-Lee scheme [12] using Eq. (29). The maximum natural circular frequency ω_{max} was determined using the regular HCB mass matrix and the linearized HCB stiffness matrix computed in Eq. (11). This method of computing the critical time step assumes a linear model, so the analysis time step Δt_a is taken as 90% of Δt_{cr} to ensure stability in the nonlinear case.

Table 3 demonstrates that the critical time step length is controlled by the HCB constraint modes computed in Eq. (5), and remains unchanged as fixed-interface modes are truncated. This suggests that HCB substructuring with nonlinear interface DOF does not gain any computational advantage directly from explicit time integration, except for the lower order of equations solved. In other words, the critical time step is determined by the constraint modes.

Table 3. HCB model comparison for different cutoff frequencies.

Cutoff FI Frequency [Hz]	FI Modes per Substructure	Max FI Frequency [Hz]	Max Model Frequency [Hz]	Model Size [DOF]	Δt_{cr} [sec]	Δt_a [sec]
2,000	4	1,544	9.14E+06	3692	3.25E-08	2.93E-08
3,000	7	2,534	9.13E+06	3698	3.25E-08	2.93E-08
4,000	8	3,763	9.13E+06	3700	3.25E-08	2.93E-08

An externally applied loading pattern $f_{ext}(t)$ was designed to excite the fundamental mode of the C-beam model, which has the displacement field shown in Figure 3a. This mode exhibits bending about the z-axis, with most of the deformation concentrated in the top beam. To excite this mode, a vertical haversine impulse was applied to a strip of nodes at center of the top C-beam. The impulse has a duration of 1 ms and was applied with various amplitudes. The loading pattern can be seen in Figure 3b.

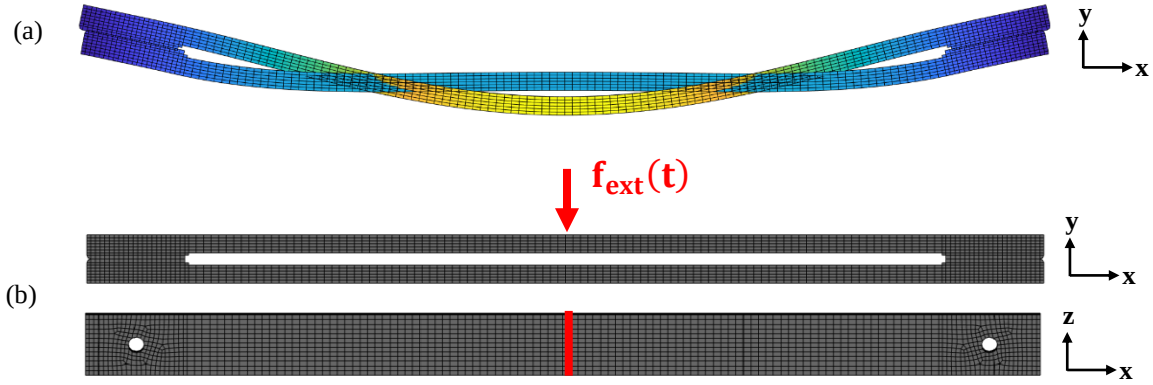

Figure 3. (a) Fundamental mode shape of the HCB model. (b) Dynamic loading pattern.

Dynamic simulation results are presented for the three HCB models described in Table 3, and for three loading amplitudes of 15 N, 100 N, and 500 N. These loading amplitudes are selected to elicit linear, moderately nonlinear, and strongly nonlinear responses, respectively. It is important to study different loading amplitudes to ensure that the HCB models retain accuracy for varying degrees of nonlinear response. A viscous damping matrix with 1% damping in all modes is included in the system to simulate a more realistic system.

Response convergence is determined based on system-level and interface-level outputs: the drive point displacement (vertical displacement at the loading point) is used to evaluate the global response convergence, while contact area

and summation of normal contact forces determine local interface-level convergence. Time histories are computed out to 10 ms to adequately show the transient vibration response of the system subjected to a 1 ms haversine impulse.

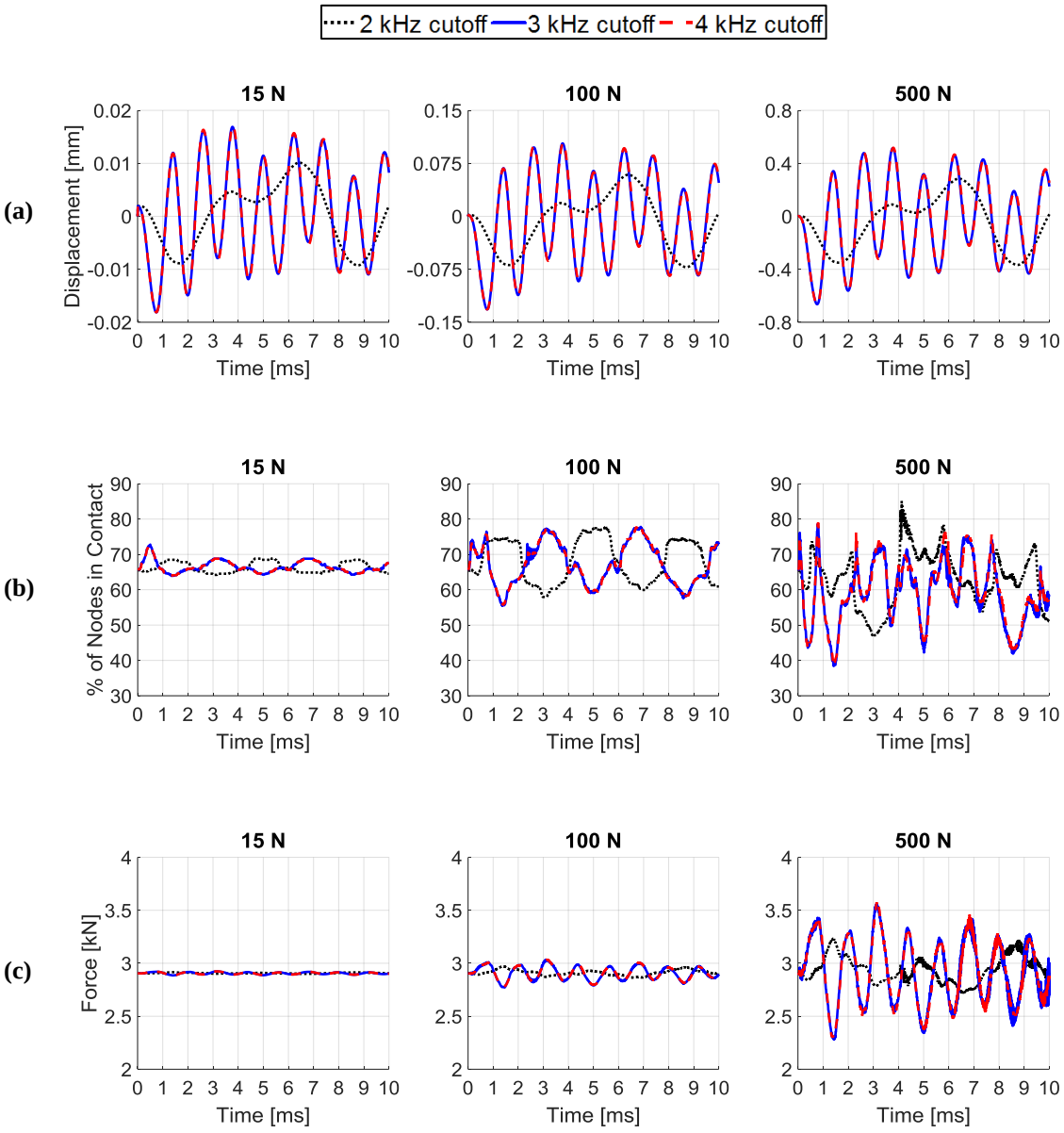

Figure 4. Time history of (a) drive point displacement; (b) contact area (percentage of nodes in contact); (c) total normal contact force on one interface. Comparison between different HCB cutoff frequencies.

A comparison of the different loading amplitudes and HCB models in Figure 4 reveals that increasing the cutoff frequency from 2 kHz to 3 kHz significantly alters the response at the system-level and interface-level. Drive point displacements, as well as contact area and interface forces, change dramatically in magnitude and frequency between the 2 kHz and 3 kHz models. Furthermore, a visual comparison shows strong similarity between the 3 kHz and 4 kHz results, indicating the reduced order models have converged. Similar to results from [4], the 2 kHz model is not accurate for this loading because the $2/\tau$ impulse frequency is 2,000 Hz, but the model only kept frequencies up to 1,544 Hz. Thus, the 2 kHz model cannot produce response frequencies in the range generated by the 1 ms impulse.

It is interesting to observe that for the 3 and 4 kHz models, the qualitative behavior of the drive point displacement does not change between different input levels (although the amplitude is scaled proportional to force). The contact area changes significantly with force level, and the total force at the interface oscillates considerably about the 2.91 kN preload force level. A seemingly linear global response in fact contains nonlinearities that are hidden in the interface-level outputs. This implies that, should friction be included, the damping characteristics of the system would change dramatically in time as the interfaces come in and out of contact.

The 3 kHz and 4 kHz models provide satisfactory starting points for interface reduction, and both would be suitable for the dynamic loading considered here. Nonetheless, the 4 kHz model provides roughly 1,200 Hz of increased frequency bandwidth over the 3 kHz model at the cost of only two more DOF, so the 4 kHz model is used for the following interface reduction studies.

3.4. Results: Interface-reduced Model

The dynamic analysis from the full-interface studies in Section 3.3 is repeated here, but now using the interface-reduced models described by Eqs. (25a) and (25b) The base HCB model includes all fixed-interface frequencies up to 4 kHz, which equates to 16 FI modes. The effect of interface fidelity is considered through several reduction cases that retain between 20 and 3,659 total SCCe modes (constrained + unconstrained). A few SCCe mode shapes with their corresponding frequencies are plotted in Figure 5 below.

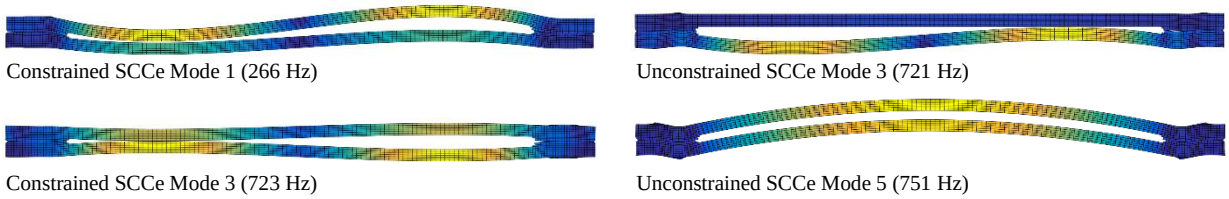

Figure 5. Amplified SCCe mode shapes. Constrained modes are formulated in Eqs. (12) and (13). Unconstrained modes are formulated in Eqs. (14) and (15).

The same process shown in Section 3.3 is employed to determine ω_{max} and Δt_{cr}, but now the eigenvalue problem is formulated in the SCCe system using $\mathbf{M}^{SCCe}$ and a linearized SCCe stiffness matrix $\mathbf{K}^{SCCe-c}$, obtained via

$$\mathbf{K}^{SCCe-c} = (\mathbf{U}^{SCCe+})^{T}\mathbf{K}^{HCB-c}\mathbf{U}^{SCCe+} \tag{30}$$

Similar to Section 3.3, the analysis time step Δt_a is obtained by multiplying the critical time step Δt_{cr} by a factor of 0.9. Table 4 summarizes the different SCCe models in terms of maximum frequency, number of DOF, and critical time step length. Note that the analysis time steps of the SCCe models are significantly larger than that of the HCB model (2.93E-08), which results in nearly an order of magnitude speed-up in explicit time solvers.

Table 4. Model comparison for various levels of SCCe interface reduction. Cases marked with * had some modes removed during the orthonormalization process.

SCCe Modes Retained	Max Constrained SCCe Frequency [Hz]	Max Unconstrained SCCe Frequency [Hz]	Max Model Frequency [Hz]	Model Size [DOF]	Δt_{cr} [sec]	Δt_a [sec]
20	1.95E+03	1.90E+03	1.87E+05	61	2.51E-07	2.26E-07
100	5.01E+04	4.18E+04	4.28E+05	141	1.37E-07	1.23E-07
200	1.12E+05	1.06E+05	5.88E+05	241	9.54E-08	8.59E-08
500	2.46E+05	2.23E+05	8.91E+05	541	6.46E-08	5.81E-08
993*	3.77E+05	3.48E+05	1.19E+06	1,034	4.37E-08	3.93E-08
3,659*	8.48E+05	7.97E+05	1.63E+06	3,700	3.26E-08	2.93E-08

Drive point displacement, contact area, and normal contact force time histories for the different SCCe models are plotted against those of the 4 kHz HCB model, shown in Figure 6.

Visual comparison of the drive point displacement histories in Figure 6a shows that all SCCe solutions lie on top of the HCB solution, with no observable deviations. For 500 or more SCCe modes, the normal contact force Figure 6c also shows near-perfect agreement. The contact area (percentage of nodes in contact) in Figure b is the slowest to converge to the HCB solution, with significant errors observed for the case of 20 and 100 SCCe modes. All results converge to the HCB solution when all SCCe modes (3,659 + 1 augmentation vector) are retained and the transformation basis is not truncated.

Drive point displacements from the HCB and SCCe models match well because the loading excites vibrational modes with deformations concentrated away from the interfaces, regardless of loading amplitude. The contact area and contact force, however, show a strong dependence on the loading amplitude. Errors in these quantities are negligible for the linear excitation of 15 N, but become more significant as the loading increases to the nonlinear excitations of 100 N and 500 N. This implies that the accuracy of the SCCe method not only depends on the number of modes in the reduction basis, but also on the degree of nonlinearity (and therefore the loading amplitude). If the only output of interest is some system-level displacement at a location sufficiently distant from the interfaces, then only a small number of SCCe modes is required. Still, the rapid changes in contact area (Figure 6b) would have a significant effect on the system-level damping if friction was included at the interface. In that case, more SCCe modes would be necessary to accurately capture system-level response.

It is important to note that at certain levels of interface reduction, the total contact force (Figure 6c) may be accurate, while the contact area (Figure 6b) has significant errors. Interface forces in the SCCe model with 500 modes show near-perfect agreement with the HCB model, but the contact areas are in error by up to 20%. A relatively small number of SCCe modes are needed for convergence in overall contact forces, but more modes must be added to achieve suitably accurate interfacial stresses, which require accurate representation of the contact area.

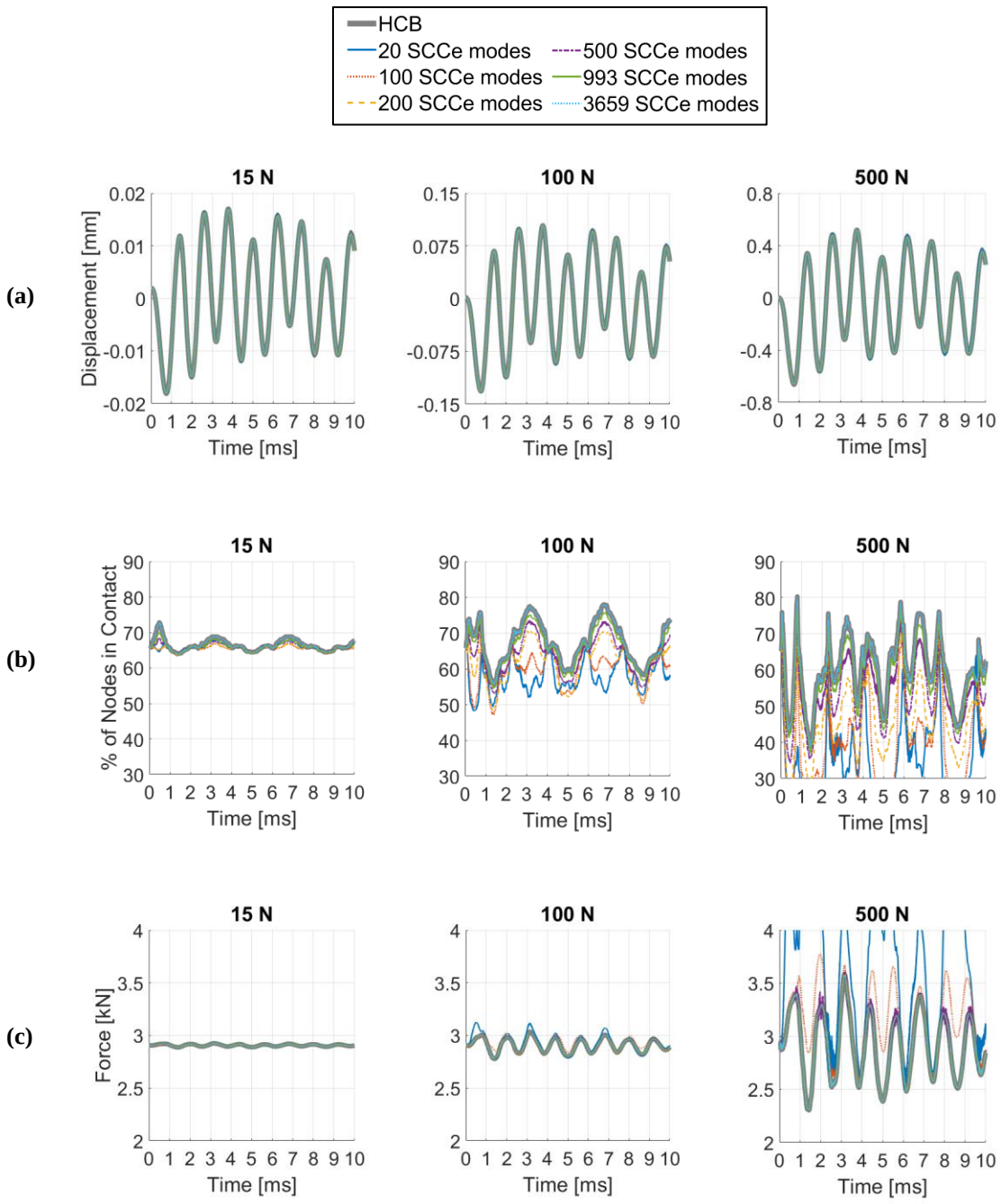

Figure 6. Time history of (a) drive point displacement; (b) contact area (percentage of nodes in contact); (c) total normal contact force on one interface. Various levels of SCCe reduction compared to full-interface HCB model.

This is confirmed by the distribution of contact forces plotted in Figure 7. The spread of contact forces over one interface surface is plotted at single instant in time (t = 3.10 ms), and under the most severe loading (500 N). At this selected time, the structure is transitioning from low to high contact area, a phenomenon that seemingly requires a high number of included SCCe modes. The sum of instantaneous contact forces quickly converges to around 3500 N, but doesn't accurately represent the distribution of those forces within the interface until many more modes are added.

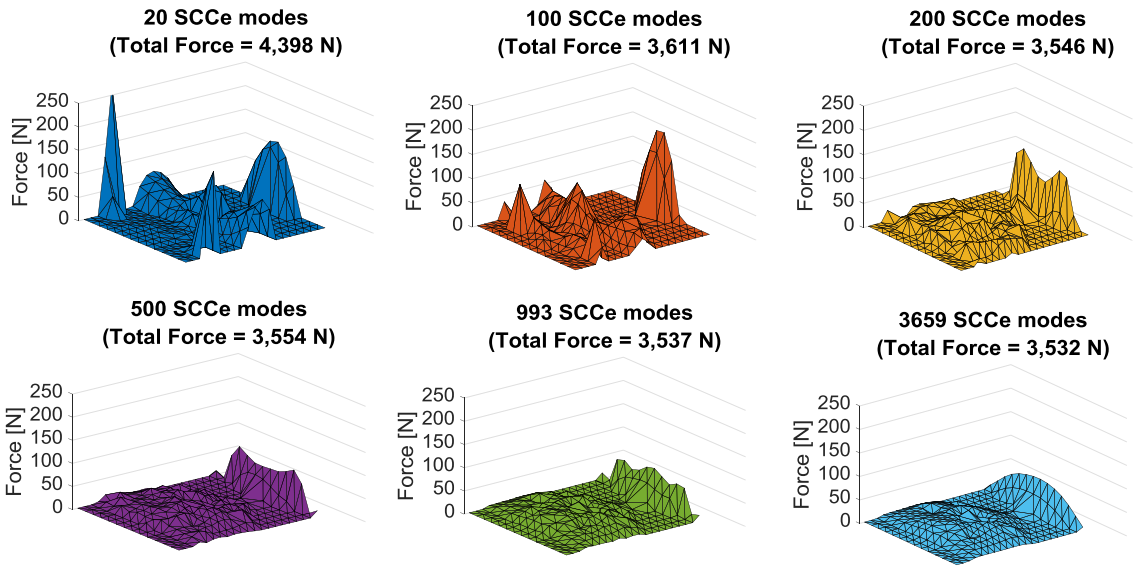

Figure 7. Contact force distribution at one interface surface for full-interface HCB model and various levels of SCCe interface reduction. Snapshot is taken at t = 3.10 ms with loading amplitude 500 N.

To the extent previously described, the interface reduction basis provides an acceptable level of accuracy relative to the full-interface HCB model. The final and arguably most important metric for gauging the effectiveness of the interface reduction is its potential for computational savings. The previous analyses were repeated using the implicit and explicit time integration schemes described in Section 2.4. Simulation run times for each of these cases are plotted in Figures 8 and 9. The solve time reduction factor is the ratio of HCB solve time to SCCe solve time.

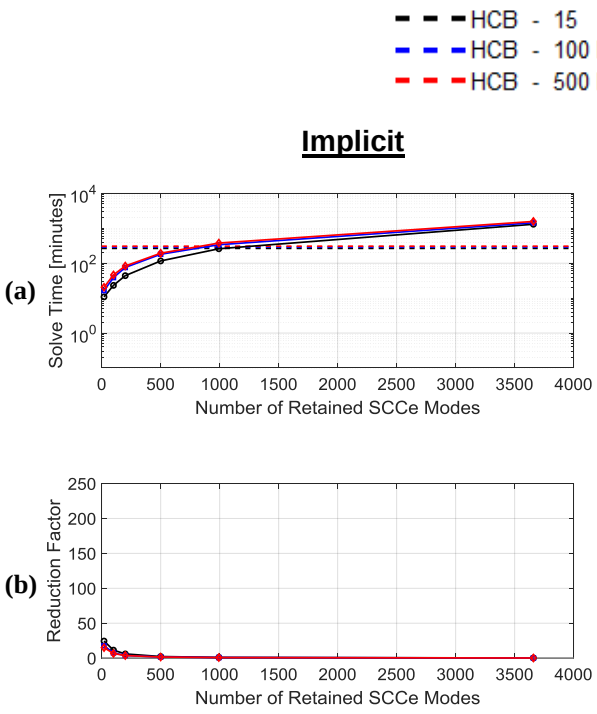

Figure 8. (a) Solve time and (b) solve time reduction factor for implicit

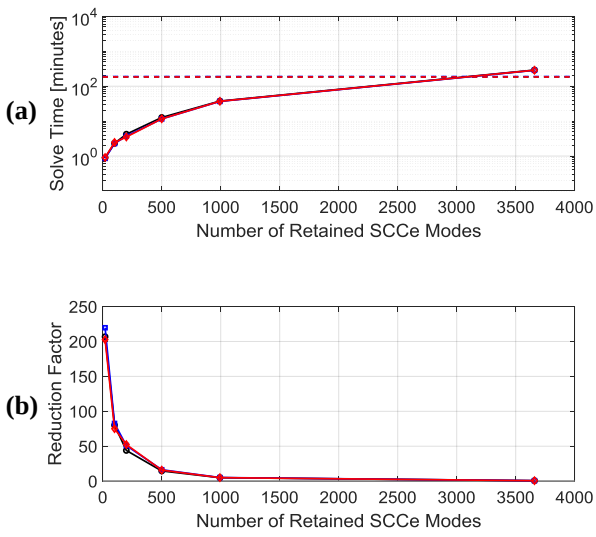

Figure 9. (a) Solve time and (b) solve time reduction factor for explicit

Explicit time integration is carried out using 90% of the critical time step as determined by Eq. (29). This resulted in a time step length of 2.93E-08 sec for the HCB model, and ranged from 2.26E-07 sec to 2.93E-08 sec for the SCCe models (see Table 4). The implicit scheme is unconditionally stable, so a time step length is chosen provide adequate resolution over a simulation time of 10 ms. For this study, a time step of 1.00E-05 sec was selected, such that the implicit scheme yields 1,000 equally-spaced solution points.

Results from the implicit simulations in Figures 8a and 8b show that the SCCe interface reduction provides a wide range of computational savings. The SCCe method reduces solve time by a factor of approximately 19 when 20 modes are included, but the savings decrease rapidly as more modes are added. With 100, 200, and 500 SCCe modes retained, the solve time is reduced by a factor of 8, 4, and 2, respectively. The 993 mode case provides almost no reduction for the 15 N loading (reduction factor of about 1), and increases solve time for the 100 N and 500 N loadings (reduction factor less than 1). The "exact" case of 3,659 SCCe more than doubles the solve time for all loading amplitudes. This seemingly counterintuitive result comes from the fact that the implicit solver requires iterations at each time step to reach equilibrium with the nonlinear contact forces. The SCCe models require a costly coordinate transformation at every state determination, so eventually the cost of performing the transformation outweighs the savings from the reduced model size. Furthermore, higher-amplitude loadings are effected more by this phenomenon because the greater degree of nonlinearity inherently requires more iterations to reach equilibrium.

The explicit simulation results in Figures 9a and 9b are drastically different than those of the implicit scheme. Firstly, the solve times are indifferent to the loading amplitude, which is due to the lower order of equations being solved relative to the implicit case. The cost savings are also much more significant, with reduction factors between 40 and 220 for the cases of 20, 100, and 200 SCCe modes. The 500 mode case reduced the computation time by a factor of 16, and the 993 mode case by a factor of 5. The cost reduction observed in the explicit results is due to the significant model size reduction (3700 reduced to 61, 141, 241, 541, or 1034), as well as the difference in time step length (see Table 4).

In the "exact" case, where 3,659 modes are retained, the SCCe simulation ran about twice as long as the equivalent HCB analysis. This means that, somewhere between 993 and 3,659 retained SCCe modes, the reduced model will complete a simulation in the same time as the full-interface model. At this critical reduction level, the benefit of a reduced model size is exceeded by the cost of the HCB-SCCe coordinate transformation that must be performed at each time step.

4. Conclusions

The Hurty/Craig-Bampton (HCB) method was applied to a system with frictionless contact, and a novel expansion of the system-level characteristic constraint mode method (SCC) method was defined and used to further reduce the model size and simulation time. The new interface reduction technique, deemed the SCCe method, reduced most of the interface DOF in the HCB model to modal DOF, while leaving some as physical DOF. Contact at the interfaces was modeled using node-to-node penalty elements in the normal direction, with the interfaces meshed such that the contact surfaces are conforming and node pairs are known a priori. The SCCe method was demonstrated on an assembly of two beams bolted together and subjected to a 1-ms haversine impulse applied at its midspan. The base HCB model used for interface reduction included 16 fixed-interface modes, with a maximum fixed-interface frequency of 3763 Hz.

Results from the SCCe reduced models indicate that only a small number of retained SCCe modes is required to reproduce system-level displacements and total contact force at the interfaces, but more SCCe modes are needed to converge to the HCB solution for contact area. Reduction in simulation time, relative to the HCB model, is most significant when using an explicit integration method. Use of an implicit scheme with the SCCe method yields much less computational savings, and even increases the simulation time where the explicit scheme would reduce it.

This research serves as a numerical proof-of-concept, which explores the viability of interface reduction on contacting substructures when nonlinear elements are applied at the interface. Results from this work indicate moderate success of the reduction scheme, but more work is needed to determine the applicability of this method to other situations. Future work will examine different reduction bases, variation in dynamic loading patterns, more general contact models, non-conforming interfaces, and the inclusion of friction elements.

Acknowledgements

This research was conducted at the 2017 Nonlinear Mechanics and Dynamics (NOMAD) Research Institute supported by Sandia National Laboratories. Sandia National Laboratories is a multi-mission laboratory managed and operated by National Technology and Engineering Solutions of Sandia, LLC., a wholly owned subsidiary of Honeywell International, Inc., for the U.S. Department of Energy's National Nuclear Security Administration under contract DE-NA-0003525.

References

[1] Gaul, L. "Wave transmission and energy dissipation at structural and machine joints." *ASME, Transactions, Journal of Vibration, Acoustics, Stress and Reliability in Design* 105 (1983): 489-496.

[2] Jenkins, G. M. "Analysis of the stress-strain relationships in reactor grade graphite." British Journal of Applied Physics 13.1 (1962): 30.

[3] Iwan, Wilfred D. "A distributed-element model for hysteresis and its steady-state dynamic response." ASME, 1966.

[4] R. J. Kuether, P. B. Coffin, and A. R. Brink. "On Hurty/Craig-Bampton Substructuring with Interface Reduction on Contacting Surfaces." Proceedings of the ASME International Design Engineering Technical Conferences & Computers and Information in Engineering Conference, 2017.

[5] Gaul, Lothar, and Jens Becker. "Damping prediction of structures with bolted joints." Shock and Vibration 17.4-5 (2010): 359-371.

[6] Hurty, Walter C. "Dynamic analysis of structural systems using component modes." AIAA journal 3.4 (1965): 678-685.

[7] Craig, Roy R., and Mervyn C. C. Bampton. "Coupling of substructures for dynamic analysis." AIAA journal 6.7 (1968): 1313-1319.

[8] D. Krattiger, L. Wu, M. Zacharczuk, M. Buck, R. J. Kuether, M. S. Allen, et al., "Interface Reduction for Hurty/Craig-Bampton Substructured Models: Review and Improvements," Mechanical Systems and Signal Processing (in review), 2017

[9] Craig Jr, Roy R., and Ching-Jone Chang. "Substructure coupling for dynamic analysis and testing." (1977).

[10] Castanier, Matthew P., Yung-Chang Tan, and Christophe Pierre. "Characteristic constraint modes for component mode synthesis." AIAA journal 39.6 (2001): 1182-1187.

[11] Wriggers, Peter. Computational contact mechanics. Springer Science & Business Media, 2006.

[12] Chung, Jintai, and Jang Moo Lee. "A new family of explicit time integration methods for linear and non-linear structural dynamics." International Journal for Numerical Methods in Engineering 37.23 (1994): 3961-3976.

[13] Crisfield, M.A., "Non-linear Finite Element Analysis of Solids and Structures. Volume 2: Advanced Topics", New York, John Wiley and Sons, pp. 455-456, 1991 Engineering & Structural Dynamics 5.3 (1977): 283-292.

[14] Sierra Structural Dynamics Development Team, "Sierra Structural Dynamics – User's Notes," SAND2017-3553, Sandia National Laboratories, Albuquerque, NM, April 2017.

[15] DIN 946 (1991-10). "Determination of coefficient of friction of bolt/nut assemblies under specified conditions." (1991).